

Compact multimode vortex-wave radiator enabled by quasi-1D spoof plasmons

Zhen Liao(廖臻), Zuquan Ao(敖祖权), Yun Li(李赟), Guo-Qing Luo(罗国清), and Leilei Liu(刘蕾蕾)
Citation: Chin. Phys. B, 2026, 35 (**8**): 084101. DOI: 10.1088/1674-1056/ae5f85
http://cpb.iphy.ac.cn; http://iopscience.iop.org/cpb

What follows is a list of articles you may be interested in

Single-beam leaky-wave antenna with wide scanning angle and high scanning rate based on spoof surface plasmon polariton

Huan Jiang(蒋欢), Xiang-Yu Cao(曹祥玉), Tao Liu(刘涛), Liaori Jidi(吉地辽日), and Sijia Li(李思佳)
Chin. Phys. B, 2022, 31 (**10**): 104101. DOI: 10.1088/1674-1056/ac5881

High-confinement ultra-wideband bandpass filter using compact folded slotline spoof surface plasmon polaritons

Xue-Wei Zhang(张雪伟), Shao-Bin Liu(刘少斌), Ling-Ling Wang(王玲玲), Qi-Ming Yu (余奇明), Jian-Lou(娄健), and Shi-Ning Sun(孙世宁)
Chin. Phys. B, 2022, 31 (**1**): 014102. DOI: 10.1088/1674-1056/ac22a2

Shared aperture metasurface antenna for electromagnetic vortices generation with different topological charges

He Wang(王贺), Yong-Feng Li(李勇峰), and Shao-Bo Qu(屈绍波)
Chin. Phys. B, 2021, 30 (**8**): 084101. DOI: 10.1088/1674-1056/abe37c

Generation of orbital angular momentum and focused beams with tri-layer medium metamaterial

Zhi-Chao Sun(孙志超), Meng-Yao Yan(闫梦瑶), and Bi-Jun Xu(徐弼军)†
Chin. Phys. B, 2020, 29 (**10**): 104101. DOI: 10.1088/1674-1056/abab79

Electromagnetic field of a relativistic electron vortex beam

Changyong Lei(雷长勇), Guangjiong Dong(董光炯)
Chin. Phys. B, 2020, 29 (**8**): 084102. DOI: 10.1088/1674-1056/ab96a9

Compact multimode vortex-wave radiator enabled by quasi-1D spoof plasmons

Zhen Liao(廖臻)[1], Zuquan Ao(敖祖权)[1], Yun Li(李赟)[2], Guo-Qing Luo(罗国清)[2], and Leilei Liu(刘蕾蕾)[1,†]

[1] *College of Electronic and Optical Engineering and College of Flexible Electronics (Future Technology), Nanjing University of Posts and Telecommunications, Nanjing* 210023, *China*

[2] *Key Laboratory of RF Circuit and System (Ministry of Education), Hangzhou Dianzi University, Hangzhou* 310018, *China*

(Received 23 December 2025; revised manuscript received 2 April 2026; accepted manuscript online 15 April 2026)

We demonstrate a compact multimode vortex-wave radiator based on quasi-one-dimensional spoof surface plasmon polaritons (quasi-1D SSPP). The structure supports simultaneous generation of four distinct orbital angular momentum modes $l = 1, -2, 3, -4$ at a single frequency. Enabled by the high propagation constant and strong field confinement of the dispersion-engineered spoof surface plasmon polaritons (SSPP) waveguide, the device achieves a footprint of only 0.9λ while maintaining high mode purity and low intermodal crosstalk. Although implemented in the microwave regime for experimental accessibility, the subwavelength corrugated geometry and slow-wave phase control mechanism are directly scalable to terahertz and infrared frequencies. This work provides a practical platform for integrated orbital angular momentum (OAM) multiplexing using planar-compatible plasmonic architectures, with potential applications in structured light generation and high-capacity photonic systems.

Keywords: orbital angular momentum, spoof surface plasmon polariton, multiple OAM radiator, compact arrays

PACS: 41.20.Jb, 73.20.Mf, 42.79.Bh, 42.50.Tx

DOI: 10.1088/1674-1056/ae5f85 **CSTR:** 32038.14.CPB.ae5f85

1. Introduction

In recent years, advancements in wireless communication technology have brought increased attention to the utilization of frequency bands. Vortex beams carrying orbital angular momentum (OAM) have garnered significant interest due to their potential to enhance communication link capacity and diversity.[1] The key reason for the capacity and efficiency improvements offered by OAM waves is the orthogonality of vortex beams with different OAM modes, enabling efficient (de)multiplexing.[2,3] Studies have also shown that OAM-carrying vortex beams contain azimuth information, making them applicable in various fields such as radar imaging,[4] micromanipulation,[5] super-resolution imaging,[6] holography,[7] precision measurement,[8] and quantum information technologies.[9,10]

Several methods have been developed to generate vortex beams, including liquid crystal Q-plates[11] and spiral phase plates.[12] However, the bulky nature of these technologies limits their integration into communication systems. To address this, planar and compact OAM radiators have been reported, including uniform circular antenna arrays,[13] multi-fed patch antennas,[14,15] circular traveling wave antennas,[16] and emission and reflection arrays.[17] Despite their compactness, these antennas require complex feeding networks and can only radiate one mode at a time. Other antenna designs, such as helical antennas,[18] have been proposed to generate multiple OAM modes, saving space and reducing costs. However, these designs often implement different OAM modes at different frequency points. To improve spectral efficiency and channel capacity, it is crucial to design antennas that generate multiple OAM modes at the same frequency. For instance, a compact slot helical antenna was designed to generate four OAM modes, but this study lacked tested phase diagrams and mode purity of OAM.[19–21]

Spoof surface plasmon polaritons (SSPP) offer new opportunities for vortex wave radiation due to their miniaturized, phase-controllable, and easily integrable properties.[22–28] Periodically modulated SSPP waveguides have been utilized to convert SSPP waves into radiated waves and generate vortex beams carrying OAM.[22–24] This approach has the advantage of a small size and simple structure, but requires frequency adjustments to generate different OAM modes. Furthermore, varactor diodes have been added to SSPP units to achieve reconfigurable OAM modes at the same frequency by changing the bias voltage.[24]

In this paper, a compact orbital angular momentum (OAM) helical radiator is presented, enabled by a quasi-one-dimensional spoof surface plasmon polariton (quasi-1D SSPP) structure.[29–31] The design employs four concentric SSPP helices with different radii, each formed by winding a quasi-1D metallic strip around a foam cylinder. The nested configu-

†Corresponding author. E-mail: liull@njupt.edu.cn

© 2026 Chinese Physical Society and IOP Publishing Ltd. All rights, including for text and data mining, AI training, and similar technologies, are reserved.

ration allows multiple OAM modes with distinct topological charges to be generated at the same frequency. The slow-wave characteristics of the SSPP line enhance phase accumulation along the helical path, enabling miniaturization of the overall diameter to only 0.9λ while maintaining strong field confinement. The high propagation constant also mitigates mutual coupling between adjacent helices, ensuring stable multimode operation. Full-wave simulations and experimental measurements confirm the generation of four azimuthally polarized modes ($l = 1, -2, 3, -4$) and four circularly polarized modes ($l = 0, -1, 2, -3$) at 3 GHz. This dispersion-engineered design provides an effective strategy for realizing compact multimode vortex radiators with promising applications in microwave communication and radar imaging.

2. Theoretical analysis

For the helical structure, where the total length of the conductor is much larger than the operating wavelength λ_0 and the turn spacing S is much smaller than λ_0, the antenna can be approximated as a linear array of circular loops with an element spacing of S, as shown in Fig. 1(a).

Here, the array factor F_{a} of the N-element uniform array can be expressed as[32]

$$F_{\mathrm{a}} = \frac{\sin\left(N\psi/2\right)}{\sin\left(\psi/2\right)}, \tag{1}$$

where progressive phase ψ is the phase difference between adjacent loops that can be represented as

$$\psi = 2\pi\left(\frac{S}{\lambda_0}\cos\theta - \frac{L/\lambda_0}{p}\right), \tag{2}$$

in which $p = v/c_0$ is the relative phase velocity of wave propagation along the helical conductor, v is the phase velocity of wave propagation along the helical conductor, and c_0 is the speed of light in free space, $L = \sqrt{S^2 + (\pi D)^2}$ is the length of a helix, D is the diameter of the helical antenna, and θ is the beam radiation angle of the helical antenna.

The circular loop carrying a traveling-wave current is illustrated in Fig. 1(b), and the current distribution on the loop can be expressed as[16]

$$I(\varphi) = I_0\,\mathrm{e}^{-\mathrm{i}l\varphi}, \tag{3}$$

in which I_0 is the current amplitude, φ varies from 0 to 2π representing the azimuth angle, l is a non-zero integer, and the circumference of the circular antenna satisfies

$$\pi D = |l|\,\lambda = |l|\,\frac{2\pi}{k}, \tag{4}$$

where λ represents the guided wavelength on the helical conductor, and k represents the propagation constant. The far-field vector potential of this circular loop can be expressed as

$$\begin{aligned}\boldsymbol{A}(\boldsymbol{r}) &= \frac{\mu I_0}{4\pi}\oint_L \frac{\mathrm{e}^{-\mathrm{i}l\varphi}\,\mathrm{e}^{-\mathrm{i}k|\boldsymbol{r}-\boldsymbol{r}'|}}{|\boldsymbol{r}-\boldsymbol{r}'|}\,\mathrm{d}l' \\ &\approx \frac{\mathrm{i}^{-l}\mu\,|r'|\,I_0\,\mathrm{e}^{-\mathrm{i}kr}\,\mathrm{e}^{-\mathrm{i}l\varphi}}{4r} \\ &\quad\times\left[\left(\hat{\boldsymbol{r}}\sin\theta + \hat{\boldsymbol{\theta}}\cos\theta - \hat{\boldsymbol{\varphi}}j\right)\mathrm{J}_{l-1}\right. \\ &\quad\left.+\left(\hat{\boldsymbol{r}}\sin\theta + \hat{\boldsymbol{\theta}}\cos\theta + \hat{\boldsymbol{\varphi}}j\right)\mathrm{J}_{l+1}\right],\end{aligned} \tag{5}$$

here J_{l-1} and J_{l+1} respectively represent $\mathrm{J}_{l-1}(ka\sin\theta)$ and $\mathrm{J}_{l+1}(ka\sin\theta)$, which are the $(l-1)$- and $(l+1)$-order Bessel functions of the first type, the radius of the circular loop antenna is $|r'| = D/2$, and r with the superscript $'$ denotes the source coordinate.

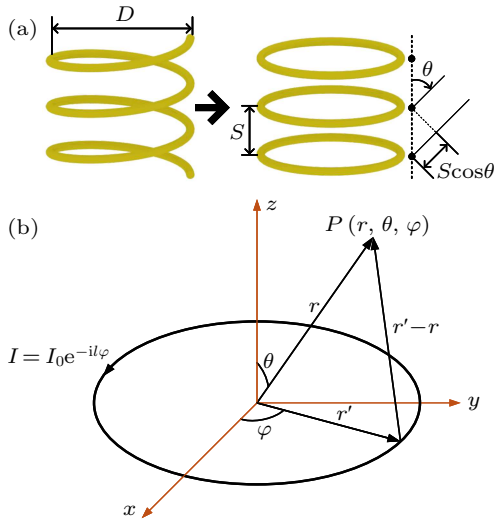


Fig. 1. (a) Helix antenna approximated as an array of circular loop carrying travelling wave current. (b) Model of a circular loop carrying travelling wave current.

Therefore, the far-field in a cylindrical coordinate is obtained as

$$\begin{aligned}E_\rho &= \frac{C}{2\omega\varepsilon}\mathrm{e}^{-\mathrm{i}kr}\,\mathrm{e}^{-\mathrm{i}l\varphi}\left\{\frac{\mathrm{i}k^2\cos^2\theta}{r}\left(\mathrm{J}_{l-1}+\mathrm{J}_{l+1}\right)+\frac{k}{r^2}\left[l\cos 2\theta\left(\mathrm{J}_{l-1}-\mathrm{J}_{l+1}\right)-\sin^2\theta\left(\mathrm{J}_{l-1}+\mathrm{J}_{l+1}\right)\right]\right\}, \\ E_\varphi &= \frac{C}{2\omega\varepsilon}\mathrm{e}^{-\mathrm{i}kr}\,\mathrm{e}^{-\mathrm{i}l\varphi}\left[\frac{k^2}{r}\left(\mathrm{J}_{l-1}-\mathrm{J}_{l+1}\right)-\frac{\mathrm{i}lk}{r^2}\left(\mathrm{J}_{l-1}+\mathrm{J}_{l+1}\right)\right], \\ E_z &= -\frac{C}{2\omega\varepsilon}\sin\theta\cos\theta\,\mathrm{e}^{-\mathrm{i}kr}\,\mathrm{e}^{-\mathrm{i}l\varphi}\left\{\frac{\mathrm{i}k^2}{r}\left(\mathrm{J}_{l-1}+\mathrm{J}_{l+1}\right)+\frac{k}{r^2}\left[\left(\mathrm{J}_{l-1}+\mathrm{J}_{l+1}\right)+2l\left(\mathrm{J}_{l-1}-\mathrm{J}_{l+1}\right)\right]\right\},\end{aligned} \tag{6}$$

where C is defined as $C = -\mathrm{i}^{-l}DI_0/4$, and the expression for the element factor F_{e} is

$$F_{\mathrm{e}} = \sqrt{|E_\rho|^2 + |E_\varphi|^2 + |E_z|^2}. \tag{7}$$

Combining Eqs. (1) and (7), the far-zone field E_{tn} can be represented as

$$E_{\mathrm{tn}} = F_{\mathrm{a}} F_{\mathrm{e}}. \tag{8}$$

This formulation clearly reveals the presence of the vortex phase factor $\mathrm{e}^{-\mathrm{i}l\varphi}$ in the far field, enabling the helical antenna to radiate an OAM beam with a topological charge l. In this configuration, the propagation constant k of the guided mode plays a key role. Increasing k effectively reduces the helical radius required for a given l, thereby achieving substantial structural miniaturization.

3. Design and analysis

The quasi-1D SSPP structure, fabricated by printing fine metallic traces on an ultrathin polyimide substrate, is illustrated in Fig. 2(a). The conventional two-dimensional (2D) SSPP structure consists of a two-dimensionally periodic groove array, as illustrated in Fig. 2(b). For the quasi-1D SSPP, the combination of an ultrathin dielectric layer and a hollow groove configuration allows the metallic waveguide to conform to curved surfaces without degrading electromagnetic confinement.[33] Figure 2(c) presents the simulated dispersion characteristics, where the structural parameters are set as: groove width $a = 1.4$ mm, period of unit $d = 3$ mm, height $H = 6$ mm, and groove depth $h = 5$ mm. The substrate has a thickness of 0.025 mm, a relative permittivity of 3.5, and a loss tangent of 0.0028. As shown in Fig. 2(c), the dispersion curve gradually deviates from the light line with increasing frequency and approaches the cut-off frequency, indicating that the quasi-1D SSPP mode is highly confined and efficiently guided along the metallic surface. Moreover, as the groove depth increases, the asymptotic frequency shifts downward, enabling continuous tuning of the propagation constant through geometric modulation. As shown in Fig. 2(d), a comparison among the quasi-1D SSPP, conventional 2D SSPP, and flat metallic strip structures with identical dimensions reveals that the quasi-1D configuration supports a significantly larger propagation constant $k_{\mathrm{1D-SSPP}}$, which promotes structural miniaturization and effectively suppresses inter-element coupling.

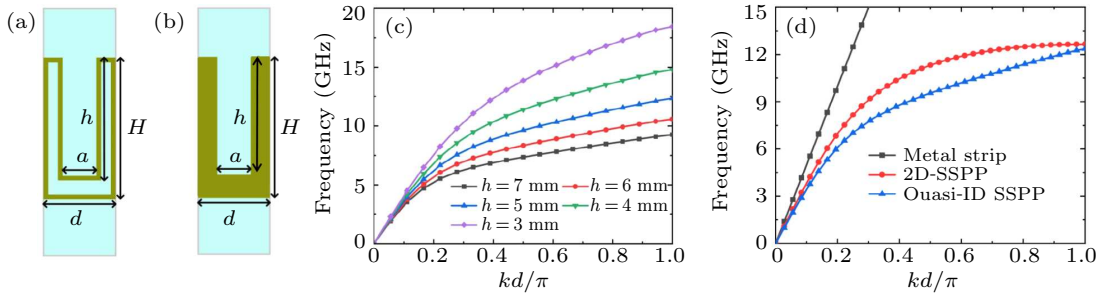


Fig. 2. (a) Unit cell of the quasi-1D SSPP structure. (b) Unit cell of the conventional 2D SSPP structure. (c) Simulated dispersion curves of the quasi-1D SSPP unit with different groove depths. (d) Comparisons of the dispersion characteristics among the quasi-1D SSPP, conventional 2D SSPP, and metallic strip structures.

To achieve a compact OAM radiator, the quasi-1D structure is employed to construct the helical antenna. The designed helical radiator operating at 3 GHz with a topological charge of $l = -4$ is shown in Fig. 3. According to Eq. (8), the relationship between the number of turns of the helical antenna and the far-field characteristics can be calculated. Considering both size and radiation performance, the flexible copper strip is wrapped twice in a right-handed direction and is composed of a metal strip joint with length L_2 and quasi-1D SSPP waveguide. The winding angle α_m is 3° and the turn spacing S is 16 mm. The antenna is fed by a 50-Ω coaxial line, with the inner conductor connected to the SSPP strip and the outer conductor soldered to a circular copper plate serving as the ground. Impedance matching is achieved using a tapered metallic transition strip with optimized dimensions of width w_m as 4.5 mm, length L_1 as 10.5 mm and height x as 7 mm. Other fixed geometric parameters include $H_a = 38$ mm, $d_1 = 1.27$ mm, $d_2 = 4.1$ mm, $D_g = 180$ mm. From the dispersion curve in Fig. 2(d), the propagation constant of the quasi-1D SSPP is $k_{\mathrm{1DSSPP}} = 90.7$ m^{-1} can be obtained at 3 GHz. According to Eq. (4), the theoretical diameter of the helix corresponding to $l = -4$ is 88.2 mm. Owing to slight deformation of the SSPP element during wrapping, the effective propagation constant of the curved structure changes slightly, and the final optimized diameter is 93.4 mm.

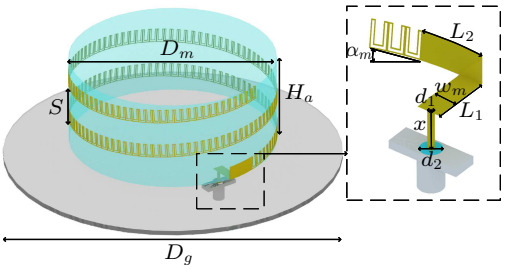


Fig. 3. Geometry of the right-handed helical antenna with an OAM mode number of −4 based on quasi-1D SSPP unit.

Figure 4(a) shows the simulated reflection coefficient of

the designed antenna. The return loss ($|S_{11}|$) remains below -10 dB within the operating band from 2.93 GHz to 3.07 GHz, confirming good impedance matching. The near-field amplitude distribution of the quasi-1D SSPP helix is plotted in Fig. 4(b), where the field gradually decays along the azimuthal direction, indicating that the plasmonic mode propagates as a right-handed traveling wave along the helical path. The handedness of this propagation determines the negative sign of the generated OAM mode. The normalized far-field radiation pattern shown in Fig. 4(c) exhibits a characteristic hollow profile with an intensity null along the boresight, consistent with the expected OAM radiation behavior. Figure 4(d) presents the phase distribution of the azimuthal electric-field component $\boldsymbol{E}_{\varphi}$, which clearly exhibits a spiral phase front at 3 GHz. The phase varies continuously along the azimuthal direction, completing a total change of -8π over one full rotation around the vortex center. This corresponds to an emitted OAM beam carrying a topological charge of $l = -4$, in agreement with the theoretical prediction.

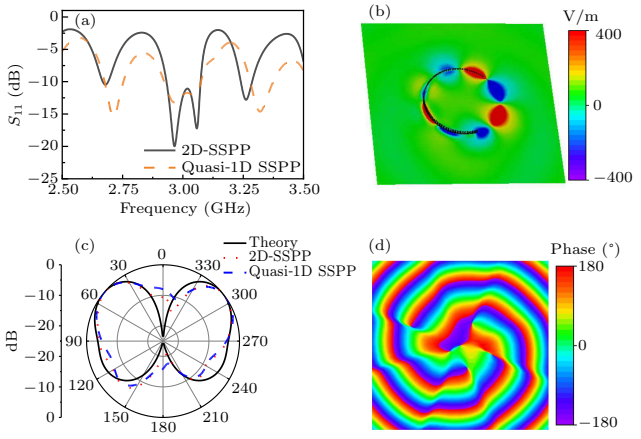


Fig. 4. (a) Simulated reflection coefficients. (b) Simulated E-field distribution at 3 GHz. (c) Simulated normalized 2D radiation patterns. (d) Simulated instantaneous phase.

As reported in Ref. [34], the conventional 2D SSPP structure can be employed to reduce the size of an axial-mode helical antenna. Owing to its higher propagation constant, the quasi-1D SSPP enables further miniaturization of the helical geometry. For comparison, 2D-SSPP helices with $D_m = 106.8$ mm and $H_a = 42$ mm were simulated, showing nearly identical impedance bandwidths and far-field radiation characteristics, as presented in Figs. 4(a) and 4(c). Under these comparable radiation conditions, the quasi-1D SSPP helix exhibits about 10% reductions in both diameter and height.

4. Multiple OAM radiation

To enhance channel capacity, a multimode OAM radiator is constructed by nesting four quasi-1D SSPP helices, each individually excited through separate feeding ports. The array operates at a single frequency of 3 GHz and simultaneously generates four distinct OAM modes. As discussed above, the quasi-1D SSPP mode exhibits a higher propagation constant, resulting in a shorter guided wavelength and stronger field confinement. Consequently, the helical elements achieve reduced diameters and improved isolation within the array.

Figure 5(a) presents a perspective view of the proposed multimode OAM antenna. To suppress crosstalk between adjacent helices, the quasi-1D SSPP structures are arranged with alternating upward and downward groove orientations. The first helix is wound in a left-handed direction, radiating a vortex beam with a topological charge of $l = 1$, while the second, third, and fourth helices are alternately wound in opposite handedness, corresponding to OAM modes of $l = -2$, 3, and -4, respectively. This alternating configuration effectively mitigates coupling caused by identical polarization states between neighboring elements. To further enhance port isolation, four coaxial feeds are symmetrically distributed around the center at 0°, 90°, 180°, and 270°, as shown in Fig. 5(b). Four helical antennas were designed, with diameters D_m of 22.3 mm, 45.6 mm, 70.5 mm, and 93.4 mm, strip widths w_m of 9 mm, 9 mm, 8 mm, and 6.5 mm, angles α_m of 12.8°, 6.4°, 4.1°, and 3.1°, and SSPP period numbers of 48, 96, 148, and 196, respectively. The simulated reflection coefficients of the four ports are shown in Fig. 5(c). Although the impedance bandwidth slightly decreases as the magnitude of the topological charge $|l|$ increases, all ports maintain $|S_{11}|$ values below -10 dB within a range of 2.92 GHz–3.06 GHz. As depicted in Fig. 5(d), the isolation between any two ports exceeds 15 dB across the entire operating band, confirming effective decoupling among the feeding channels.

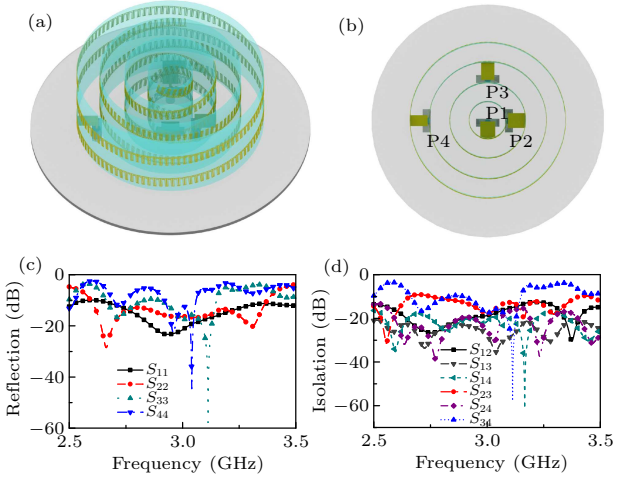


Fig. 5. (a) Perspective and (b) bottom views of the OAM helical antenna model. Simulated reflection (c) and isolation (d) coefficients of the proposed OAM antenna.

For experimental verification, a prototype of the four-mode quasi-1D SSPP helical antenna was fabricated and characterized. Photographs of the fabricated prototype are shown

in Fig. 6(a). The quasi-1D SSPP metallic traces were patterned on a polyimide film and subsequently wrapped around a polymethacrylimide (PMI) foam cylinder with a relative permittivity of 1.07 and a loss tangent of 0.0005. Each antenna element was fed through an SMA connector mounted on the side of the metallic ground plane and soldered to the matching strip. The radiation patterns and near-field distributions were measured in a microwave anechoic chamber, as shown in Figs. 6(b) and 6(c).

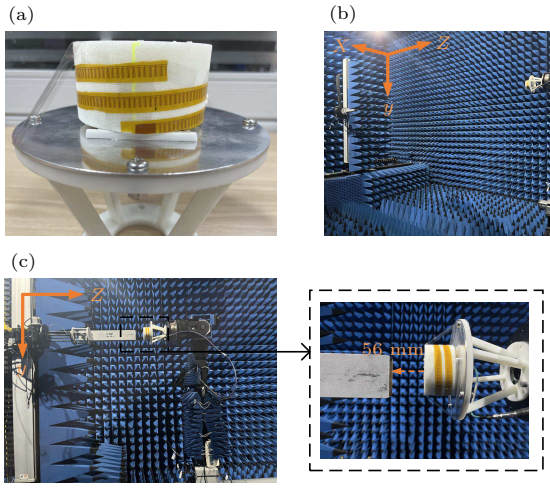


Fig. 6. (a) Prototype antenna, (b) far field gain, and (c) near field testing environment.

The measured reflection coefficients are presented in Fig. 7(a). The operating bandwidth decreases as the topological charge number increases, similar to the simulation results. The −10-dB bandwidth of the four ports is observed to be 2.62 GHz–3.5 GHz, 2.6 GHz–3.37 GHz, 2.9 GHz–3.15 GHz, and 2.92 GHz–3.06 GHz, respectively. The center frequency shifts to 2.85 GHz from the simulated 3 GHz, primarily due to the relative dielectric constant of the foam material, which was not accounted for in the simulation. As displayed in Fig. 7(b), the test results show that the isolation between helical antennas is below −15 dB at 2.85 GHz, indicating good isolation.

We investigated the electric field in the near-field zone. An open-ended waveguide is used as the receiving probe. The probe is mounted on a 2D scanning platform and records the complex electric field distribution point by point across the x–y plane, as shown in Fig. 6(c). By rotating the waveguide probe, both x- and y-polarized electric field components (E_x and E_y) are measured. To ensure that the measured fields accurately reflect the near-field performance of the OAM antenna, the distance between the transmitting OAM antenna and the receiving probe is set to[35]

$$R = \sqrt{\frac{D^3}{\lambda}} \approx 56\ \text{mm}. \tag{9}$$

We record the electric field components (E_x, E_y) and transform them into cylindrical coordinates to obtain the azimuthal component E_φ, which is given by: $E_\varphi = -E_x \sin(\varphi) + E_y \cos(\varphi)$. The phase distribution is extracted from the complex azimuthal component E_φ of the vector electric field as

$$\psi(r, \varphi) = \arg[E_\varphi(r, \varphi)]. \tag{10}$$

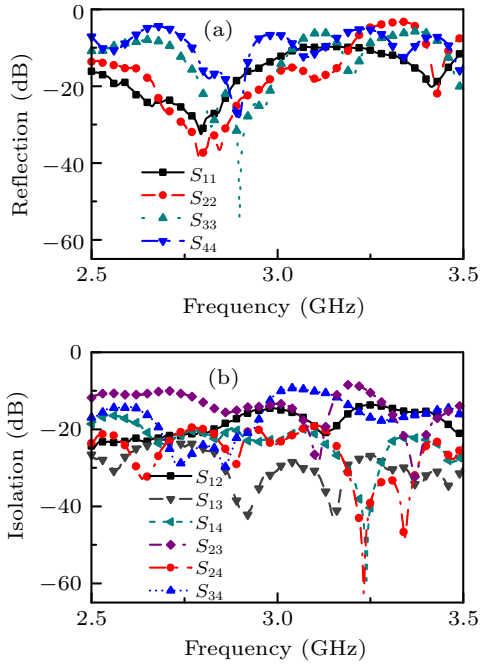


Fig. 7. (a) Measured reflection and (b) isolation coefficients of the proposed OAM antenna.

Figures 8(a) and 8(b) present the simulated and measured E_φ phase distributions of the proposed OAM antenna. Spiral phase fronts are clearly observed for all four helical antennas. Phase variations of 2π, -4π, 6π, and -8π correspond to the $l = 1$, -2, 3, and -4 OAM modes, respectively. The measured phase results are in good agreement with simulations. Figure 8(c) presents the measured E_φ intensity distributions of the proposed OAM antenna. A hollow region is observed at the center of the electric field intensity distribution, and as the mode order increases, the hollow region expands accordingly, which is as expected. To quantify the mode purity, we perform an angular Fourier decomposition of E_φ along a closed circular contour[36]

$$A_l = \frac{1}{2\pi} \int_0^{2\pi} \psi(\phi)\, \mathrm{e}^{-\mathrm{i}l\phi}\, \mathrm{d}\phi, \tag{11}$$

where $\psi(\phi)$ is the azimuthal phase sampled from the near-field data. Figure 8(d) shows the OAM mode purities for the simulated results. The $l = 1$ and -2 modes exceed 95%, the $l = 3$ mode is above 85%, and the $l = -4$ mode is approximately 70%, demonstrating that all generated vortex beams possess high purity.

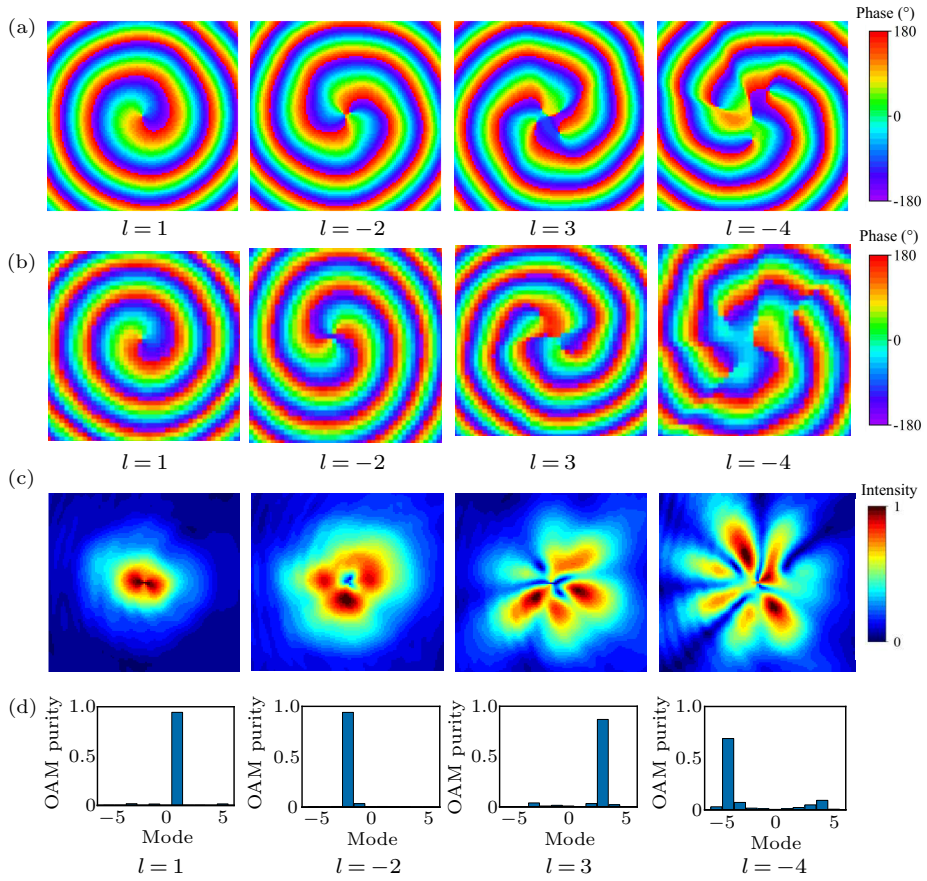


Fig. 8. Simulated (a) and measured (b) electric field phase at 3 GHz, (c) measured electric field intensity at 3 GHz, (d) OAM purity weight for the simulated results.

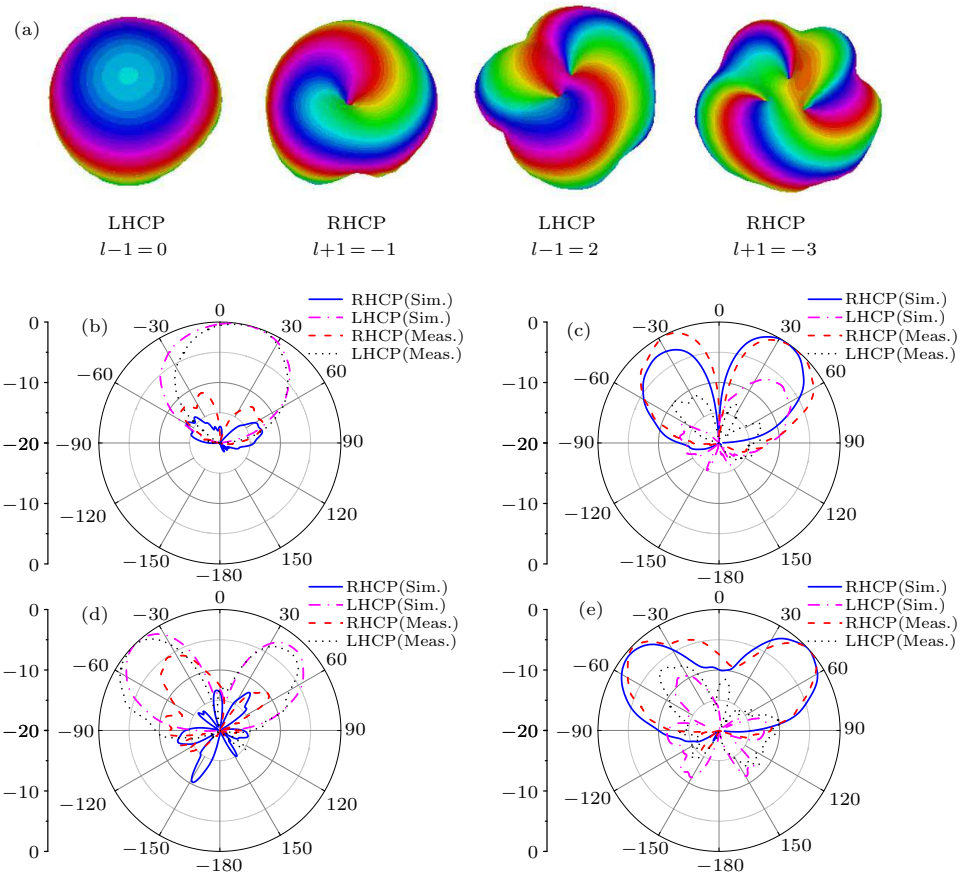


Fig. 9. (a) Simulated three-dimensional (3D) far-field LHCP and RHCP phase results of the helical antenna. Measured and simulated far-field results of (b) $l=0$, (c) $l=-1$, (d) $l=2$, (e) $l=-3$.

The azimuthal electric field component E_φ can be expressed as a combination of left-hand circularly polarized (LHCP) and right-hand circularly polarized (RHCP) components. Thus, the E_φ vector vortex (VV) beams of topological charge l can be decomposed into two scalar vortices (SVs) as follows:

$$E_\varphi = E_0 \mathrm{e}^{-\mathrm{i}l\varphi}\hat{\boldsymbol{\varphi}} = -\frac{\mathrm{j}}{2}\left[-E_0\left(\hat{\boldsymbol{x}}-\mathrm{i}\hat{\boldsymbol{y}}\right)\mathrm{e}^{-\mathrm{i}(l-1)\varphi} + E_0\left(\hat{\boldsymbol{x}}+\mathrm{i}\hat{\boldsymbol{y}}\right)\mathrm{e}^{-\mathrm{i}(l+1)\varphi}\right]. \quad (12)$$

It is observed that the LHCP vortex beam carries OAM of $l+1$, while the RHCP scalar beam carries OAM of $l-1$. This property provides additional design flexibility for the proposed OAM antenna. Owing to the intrinsic characteristics of the helical antenna, the dominant circular polarization of the radiated wave follows the handedness of the helix. Accordingly, the four antenna ports primarily emit LHCP, RHCP, LHCP, and RHCP waves, respectively.

The simulated far-field phase distributions with multiple modes are shown in Fig. 9(a). As expected, the LHCP far-field phase patterns of the first and third antennas are clear, exhibiting 0 and 4π phase variations, respectively, while the second and fourth antennas primarily radiate RHCP waves with OAM modes of -1 and -3, respectively. Figures 9(b)–9(e) compare the simulated and measured results for the RHCP and LHCP patterns of the proposed OAM antenna in four modes. The simulation results are at 3 GHz, while the measured results are at 2.85 GHz. The co-polarization radiation performance of each helical antenna aligns with its handedness. Port 1 exhibits a conventional LHCP beam in the boresight direction, corresponding to charge 0. The radiation patterns of the higher OAM modes show amplitude nulls in the central region. As the mode order increases, the angular separation between the lobes increases, reducing directivity. The difference between the co-polarization and the cross-polarization at the maximum radiation angles indicates that all the OAM modes exhibit certain co-circular polarization radiation. Figure 10 illustrates the simulation results of the OAM antenna axis ratio (AR). At the maximum radiation angle, the AR for all the OAM modes is below 3 dB, indicating good circular polarization performance.

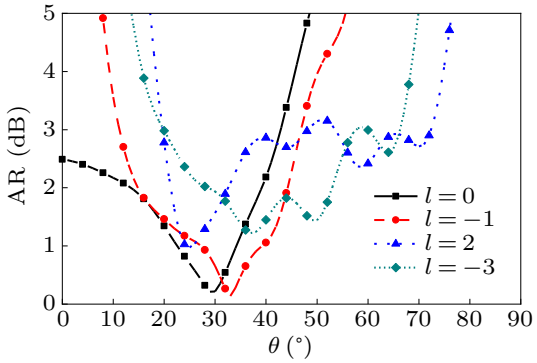


Fig. 10. Simulated AR results of the proposed OAM antenna.

Table 1. Comparisons of the proposed antenna with the results of similar OAM antennas.

Ref.	Operating approach	Size (λ_0)	OAM modes	Frequency	Gain (dBi)
[15]	microstrip	0.4	0, −2, 4 (CP)	multiple Freq.	< 5
[19]	helical	1.04	0, −1, −2, −3 (CP)	single Freq.	N. A.
[24]	2D SSPP	1.37	−1, 0, 1 (LP)	single Freq.	N. A.
This work	quasi-1D SSPP	0.93	0, −1, 2, −3 (CP)	single Freq.	8.54, 7.46, 6.87, 4.65

Table 1 compares the proposed OAM antenna with existing multimode OAM antennas in terms of antenna operating approach, size, OAM mode, frequency, and gain. The proposed antenna achieves four circularly polarized OAM modes, featuring a more compact size than most reported multimode OAM antennas while achieving higher gain. The compactness, high gain, and multimode capability of the proposed antenna provide a significant advantage, allowing for integration with the OAM transmitter and receiver.

5. Conclusion

In summary, a nested helical antenna utilizing a quasi-1D SSPP structure has been developed to generate multiple OAM beams at a working frequency of 3 GHz. This work establishes a dispersion-engineered platform for compact OAM radiation, demonstrating an effective route for multiplexed vortex-wave generation. A key limitation of the current design is the lack of collinear OAM beam generation. Future work will explore approaches to achieve collinearity, such as wavefront shaping with metasurfaces or adjusting the SSPP waveguide angle to align the radiation directions. In addition, future work will focus on system-level evaluation, including channel crosstalk, capacity, and multi-channel communication performance under simultaneous multi-port excitation, through the establishment of a dedicated multi-channel transmitting and receiving platform.

Acknowledgements

Project supported by the National Key Research and Development Program of China (Grant No. 2025YFE0204200), the National Natural Science Foundation of China (Grant Nos. 62371255, 62125105, and U24A20223), the Natural

Science Research Start-up Foundation of Recruiting Talents of Nanjing University of Posts and Telecommunications (Grant No. NY223153), and the Postgraduate Research & Practice Innovation Program of Jiangsu Province (Grant No. KYCX25_1123).

References

[1] Tamburini F, Mari E, Sponselli A, Thidé B, Bianchini A and Romanato F 2012 *New J. Phys.* **14** 033001

[2] Yan Y, Xie G, Lavery M P J, Huang H, Ahmed N, Bao C, Ren Y, Cao Y, Li L, Zhao Z, Molisch A F, Tur M, Padgett M J and Willner A E 2014 *Nat. Commun.* **5** 4876

[3] Xu C, Zheng S, Zhang W, Chen Y, Chi H, Jin X and Zhang X 2016 *IEEE Microw. Wirel. Compon. Lett.* **26** 738

[4] Liu K, Cheng Y, Li X, Qin Y, Wang H and Jiang Y 2016 *IEEE Antennas Wirel. Propag. Lett.* **15** 1873

[5] Padgett M and Bowman R 2011 *Nat. Photon.* **5** 343

[6] Franke-Arnold S, Allen L and Padgett M 2008 *Laser Photon. Rev.* **2** 299

[7] Han F F, Wang Z W, Wang L and Zhao S M 2025 *Chin. Phys. B* **34** 054204

[8] Ji J Y, Zheng Z G, Zhu J L, Wang L, Wang X G and Zhao S M 2024 *Chin. Phys. B* **33** 014204

[9] Chen L, Lei J and Romero J 2014 *Light Sci. Appl.* **3** e153

[10] Cao Z W, Wang Y J, Chai G, Chen X L and Lu Y 2025 *Chin. Phys. B* **34** 020308

[11] Cardano F, Karimi E, Slussarenko S, Marrucci L, de Lisio C and Santamato E 2012 *Appl. Opt.* **51** C1

[12] Wei W, Mahdjoubi K, Brousseau C and Emile O 2016 *IET Microw. Antennas Propag.* **10** 1420

[13] Yang Z, Zhou J, Kang L, Liu B, Yang G and Shi X 2020 *IEEE Antennas Wirel. Propag. Lett.* **19** 2492

[14] Huang Y, Li X, Li Q, Qi Z, Zhu H, Akram Z and Jiang X 2019 *Sci. Rep.* **9** 12977

[15] Yang Y, Shen F, Tian L and Liu B 2024 *IEEE Antennas Wirel. Propag. Lett.* **23** 3451

[16] Zheng S, Hui X, Jin X, Chi H and Zhang X 2015 *IEEE Trans. Antennas Propag.* **63** 1530

[17] Chen G T, Jiao Y C and Zhao G 2019 *IEEE Antennas Wirel. Propag. Lett.* **18** 182

[18] Shen F, Mu J, Guo K, Wang S and Guo Z 2019 *IEEE Antennas Wirel. Propag. Lett.* **18** 1091

[19] Koohkan E, Jarchi S, Ghorbani A and Bod M 2023 *IEEE Antennas Wirel. Propag. Lett.* **22** 527

[20] Weiguo D, Yongzhong Z, Yang Y and Kaiwei Z 2018 *IEEE Access* **6** 57056

[21] Yang Y, Guo K, Shen F, Gong Y and Guo Z 2019 *IEEE Access* **7** 138541

[22] Yin J Y, Ren J, Zhang L, Li H and Cui T J 2018 *Laser Photonics Rev.* **12** 1600318

[23] Liao Z, Zhou J N, Luo G Q, Wang M, Sun S, Zhou T, Ma H F, Cui T J and Liu Y 2020 *Phys. Rev. Appl.* **13** 054013

[24] Liao Z, Che Y, Liu L, Pan B C, Cai B G, Zhou J N, Luo G Q and Liu Y 2022 *IEEE Trans. Antennas Propag.* **70** 6795

[25] Feng H, Ye L, Zhang Y, Li W, Chen H and Liu Q H 2020 *Appl. Phys. Lett.* **117** 241601

[26] Su G, Su H, Hu L, Qin Z, Shen X, Ding J, Liu F, Lu M, Zhan P and Liu Y 2021 *Appl. Phys. Lett.* **118** 241106

[27] Feng H, Zhang Z, Fu J, Zhang Q and Zhang K 2024 *IEEE Trans. Antennas Propag.* **72** 1150

[28] Fu Q, Ni H, Luo G Q, Zhu L and Liu L 2023 *IEEE Trans. Antennas Propag.* **71** 50

[29] Pendry J B, Martín-Moreno L and Garcia-Vidal F J 2004 *Science* **305** 847

[30] Shen X, Cui T J, Martin-Cano D and Garcia-Vidal F J 2013 *Proc. Natl. Acad. Sci. USA* **110** 40

[31] Ma H F, Shen X, Cheng Q, Jiang W X and Cui T J 2014 *Laser Photonics Rev.* **8** 146

[32] Balanis C A 2016 *Antenna Theory: Analysis and Design* (New York: Wiley) pp. 120–135

[33] Zu H R, Wu B, Chen B, Li W H, Su T, Liu Y, Tang W X, He D P and Cui T J 2023 *Nat. Electron.* **6** 525

[34] Cheng Z W, Deng J, Wang M, Chen J R, Wang S, Luan S, Liu X, Gao F, Ma H F and Cui T J 2023 *IEEE Trans. Antennas Propag.* **71** 5582

[35] Yang G, Zhang L, Li W W and Liu Q H 2021 *AIP Adv.* **11** 115204

[36] Yao E, Franke-Arnold S, Courtial J, Barnett S and Padgett M 2006 *Opt. Express* **14** 9071